

WGAST: Weakly-Supervised Generative Network for Daily 10 m Land Surface Temperature Estimation via Spatio-Temporal Fusion

Sofiane Bouaziz, *Student Member, IEEE*, Adel Hafiane, *Member, IEEE*, Raphaël Canals, Rachid Nedjai

Abstract—Urbanization, climate change, and agricultural stress are increasing the demand for precise and timely environmental monitoring. Land Surface Temperature (LST) is a key variable in this context and is retrieved from remote sensing satellites. However, these systems face a trade-off between spatial and temporal resolution. While spatio-temporal fusion methods offer promising solutions, few have addressed the estimation of daily LST at 10 m resolution. In this study, we present WGAST, a weakly-supervised generative network for daily 10 m LST estimation via spatio-temporal fusion of Terra MODIS, Landsat 8, and Sentinel-2. WGAST is the first end-to-end deep learning framework designed for this task. It adopts a conditional generative adversarial architecture, with a generator composed of four stages: feature extraction, fusion, LST reconstruction, and noise suppression. The first stage employs a set of encoders to extract multi-level latent representations from the inputs, which are then fused in the second stage using cosine similarity, normalization, and temporal attention mechanisms. The third stage decodes the fused features into high-resolution LST, followed by a Gaussian filter to suppress high-frequency noise. Training follows a weakly supervised strategy based on physical averaging principles and reinforced by a PatchGAN discriminator. Experiments demonstrate that WGAST outperforms existing methods in both quantitative and qualitative evaluations. Compared to the best-performing baseline, on average, WGAST reduces RMSE by 17.05% and improves SSIM by 4.22%. Furthermore, WGAST effectively captures fine-scale thermal patterns, as validated against near-surface air temperature measurements from 33 near-ground sensors. The code is available at <https://github.com/SofianeBouaziz1/WGAST.git>.

Index Terms—Spatio-temporal fusion, land surface temperature, spatial resolution, temporal resolution, generative adversarial networks.

I. INTRODUCTION

CLIMATE change, rapid urbanization, and increasing environmental pressures are reshaping the dynamics of our planet with unprecedented speed [1]. Cities are expanding both in size and density, which makes issues like the Urban Heat Island (UHI) effect even worse [2]. At the same time, unpredictable weather patterns and changing ecosystems demand consistent attention and monitoring [3]. These phenomena are

spatially and temporally complex, and tackling them requires reliable, fine-grained geospatial information with dense temporal frequency [4]. Such information is essential for sustainable urban planning [5], public health [6], disaster response [7], and climate adaptation [8]. In this context, access to high-resolution environmental data is not only beneficial but crucial for making timely and informed decisions [9].

Land Surface Temperature (LST) is a key geophysical variable for understanding and analyzing diverse environmental challenges. It represents the radiative skin temperature of the land surface, reflecting interactions among solar radiation, land cover, and atmospheric conditions [10]. LST is widely used in climate change studies [11], natural resource management [12], and urban planning [13]. It is recognized by NASA [14] and the Global Climate Observing System [15] as an essential Earth system and climate variable. Remote sensing (RS) satellites are the primary means for monitoring LST at regional to global scales [16]. They retrieve LST via thermal infrared (TIR) sensors that measure emitted radiation from the Earth’s surface [17]. Current RS satellites face a trade-off between spatial and temporal resolution [17], [18]. Spatial resolution refers to the level of surface detail captured within each LST pixel [17], while temporal resolution indicates how often LST data are acquired for the same geographic area over time [18]. For example, Terra MODIS provides daily LST at 1 km resolution, whereas Landsat 8 offers 30 m resolution but revisits every 16 days the same area. Fig.1 illustrates this trade-off, by showing that fine spatial features, such as the Loire River, France’s longest, are visible on Landsat 8 but not on Terra MODIS, and that 16 daily Terra MODIS acquisitions occur between two Landsat 8 observations. Achieving both high spatial and temporal resolution remains challenging but essential for capturing dynamic phenomena.

To overcome this limitation, Spatio-Temporal Fusion (STF) techniques have emerged as a promising solution. They generate high spatial resolution satellite observations at finer temporal frequencies by combining data from RS satellites with complementary characteristics [19], typically one with high spatial but low temporal resolution (HSLT) and another with low spatial but high temporal resolution (LSHT) [20]. STF was initially developed for fine-resolution surface reflectance (SR) imagery [19], [21], but has proven effective for LST estimation [9]. Existing STF methods fall into two main categories: traditional and learning-based. Traditional methods include weighted-based, unmixing-based, and hybrid approaches, with weighted-based being the most common. They predict fine-

This work was supported by Orléans Métropole and Région Centre-Val de Loire. (Corresponding author: Sofiane Bouaziz).

Sofiane Bouaziz is with INSA CVL, PRISME UR 4229, Bourges, 18022, Centre Val de Loire, France (e-mail: sofiane.bouaziz@insa-cvl.fr).

Sofiane Bouaziz, Raphaël Canals, and Adel Hafiane are with Université d’Orléans, PRISME UR 4229, Orléans, 45067, Centre Val de Loire, France (e-mail: raphael.canals@univ-orleans.fr; adel.hafiane@univ-orleans.fr).

Rachid Nedjai is with Université d’Orléans, CEDETE, UR 1210, Orléans, 45067, Centre Val de Loire, France (e-mail: rachid.nedjai@univ-orleans.fr).

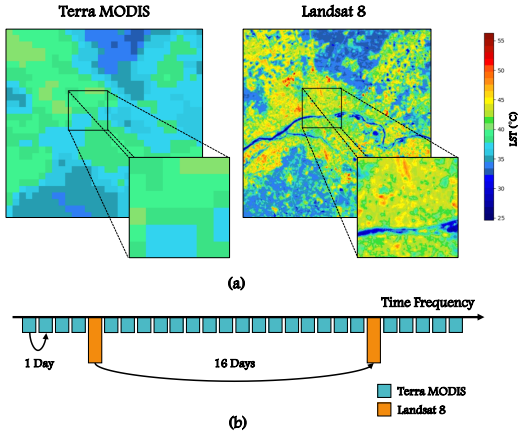


Fig. 1. LST resolution comparison over Orléans Métropole, France. (a) Spatial resolution difference between Terra MODIS and Landsat 8 on 13 Aug 2022. (b) Temporal resolution illustrated by the satellites’ revisit frequencies.

resolution images using spectrally similar neighboring pixels. Notable examples include STARFM [22], which uses moving windows and spatial similarity to estimate high-resolution observations. Its enhanced version, ESTARFM [23], further improves fusion by distinguishing between mixed and pure pixels. Although designed for SR data, these methods have been adapted for LST. For instance, Liu et al. [24] applied STARFM to fuse Terra MODIS and ASTER data and generate ASTER-like LST, and Ma et al. [25] employed ESTARFM to blend Terra MODIS and Landsat 8 for producing 100 m LST. However, traditional methods rely on the assumption that surface changes are linear over time. This assumption may hold for SR, but fails to capture the non-linear and dynamic nature of LST [26]. Consequently, traditional methods often struggle to model the spatio-temporal variability of LST with sufficient accuracy. To address this, Yu et al. [27] proposed unbiased ESTARFM, an improved variant of ESTARFM to generate daily 100 m LST while accounting for high temporal dynamics. It introduces a bias correction to reduce temperature deviations between coarse and fine observations. Gao et al. [28] also applied ESTARFM to produce daily 30 m LST and refined it using a random forest with auxiliary variables, such as spectral indices and topography.

Learning-based methods remove the linear assumption by using data-driven models to capture complex spatio-temporal relationships between LSHT and HSLT LST. With advances in deep learning (DL), these approaches have become the most widely used for STF. For example, Yin et al. [29] proposed STTFN, a residual multiscale convolutional neural network to estimate fine-resolution LST. Chen et al. [30] employed a conditional variational autoencoder framework to generate fine-resolution LST. More recently, Hu et al. [31] developed a two-stage hierarchical fusion model based on the Swin Transformer for enhanced LST estimation.

Among recent trends, generative adversarial networks (GANs) [32] have shown notable success in image generation, including STF. In this setting, the generator produces high-resolution fused images, while the discriminator distinguishes them from real high-resolution samples, thus improving re-

alism and fidelity. Several GAN-based STF approaches have been proposed. For example, STFGAN [33] frames the STF task as a super-resolution problem. GAN-STFM [34] extends this approach by introducing conditional constraints, which enable a more flexible and context-aware fusion process. CycleGAN-STF [35] treats STF as a data augmentation task and selects the most informative image from cycle-consistent outputs as the final fusion result. MLFF-GAN [36] adopts a multilevel conditional GAN (cGAN) to model spatio-temporal dependencies. However, these methods were designed and validated for SR datasets. Direct application to LST is challenging due to fundamentally different spatio-temporal dynamics [37]. SR changes with vegetation and seasons, but its daily variation is limited by slow solar illumination. In contrast, LST can vary rapidly, even hourly, due to weather, solar radiation, wind, and other environmental factors [38]. Spatially, LST can vary sharply over short distances (e.g., streets, roofs, vegetation), whereas SR changes more gradually with vegetation and seasonal cycles [38]. Consequently, GAN-based STF methods require architectural and methodological adjustments to handle LST’s rapid spatio-temporal variability.

All of the aforementioned STF methods generate fused LST at the minimum spatial resolution of the input satellites, which, at best, is 30 m from Landsat 8 [39]. Thus, both traditional and learning-based STF methods must rely on Landsat 8 as the highest-resolution thermal reference, which restricts their fusion outputs to its native spatial scale. Moreover, most DL-based STF architectures are designed for specific sensor pairs (e.g., Terra MODIS–Landsat 8) and do not generalize easily to heterogeneous optical sensors. While sufficient for some applications, the 30 m resolution is inadequate for studies requiring very high spatial precision, such as UHI analysis, which requires high spatial resolution around 10 m to capture intraurban temperature variations and narrow features like streets and small green spaces [40], [41]. Recent attempts to generate daily 10 m LST include [42], which combines Terra MODIS and Sentinel-2 with robust least squares regression, and [43], which introduces mDTSG to fuse Terra MODIS and Sentinel-2 via a convolution-based moving window. However, both approaches remain traditional STF methods and rely on the same linearity assumptions discussed earlier, which limit their ability to model complex spatio-temporal LST dynamics. Additionally, transitioning from 1 km Terra MODIS to 10 m Sentinel-2 represents a 100× increase in detail. Direct fusion without an intermediate resolution step amplifies noise, inconsistencies, and may produce unrealistic spatial patterns. Despite this, learning-based DL methods for daily 10 m LST remain largely unexplored. The only attempt, FuseTen [44], uses a hybrid model that combines a cGAN with linear regression by embedding a linear model within the generator, which can introduce artifacts and noise in the generated LST.

In this work, we address the identified research gap by introducing WGAST, a weakly-supervised generative network for daily 10 m LST estimation via STF. To the best of our knowledge, WGAST is the first non-linear end-to-end DL model that simultaneously fuses Terra MODIS, Landsat 8, and Sentinel-2 to produce daily 10 m LST. Our key contributions are summarized as follows:

- We propose a feature fusion mechanism that integrates cosine similarity, normalization, and temporal attention to effectively fuse multi-source satellite features.
- We introduce a hierarchical approach that employs Landsat 8 as an intermediate resolution bridge to overcome the extreme 1 km to 10 m resolution gap.
- We develop a weak supervision strategy that leverages 30 m Landsat 8-derived LST to compensate for the lack of 10 m ground truth.

II. PROBLEM FORMULATION

The STF problem for estimating daily 10 m LST can be formulated as follows. Let X_1 , X_2 , and X_3 denote three RS satellites with complementary spatial and temporal resolutions. We define $r_s(\cdot)$ and $r_t(\cdot)$ as the spatial and temporal resolution functions, respectively, and $\text{TIR}(\cdot)$ as a binary indicator that equals 1 if the RS satellite provides TIR observations and 0 otherwise. The following conditions in Equation 1 must hold.

$$\begin{aligned} r_s(X_1) > r_s(X_2) > r_s(X_3), \quad r_t(X_1) < r_t(X_2) \\ r_s(X_3) = 10 \text{ m}, \quad r_t(X_1) = 1 \text{ day} \\ \text{TIR}(X_1) = \text{TIR}(X_2) = 1 \end{aligned} \quad (1)$$

In our configuration, X_1 corresponds to Terra MODIS (1 km, 1 day), X_2 to Landsat 8 (30 m, 16 days), and X_3 to Sentinel-2 (10 m, 5 days), as summarized in Table I. This formulation is general and can be extended to other RS missions that meet the conditions in Equation 1.

TABLE I
COMPARISON OF REPRESENTATIVE RS SATELLITES WITH THEIR THERMAL SENSORS, SPATIAL AND TEMPORAL RESOLUTIONS.

Satellite	Thermal sensor	Spatial resolution	Temporal resolution
Terra	MODIS	1 km	1 day
Landsat 8	TIRS	30 m	16 days
Sentinel-2	/	10 m	5 days

Given a target date t_2 , the goal is to estimate LST at 10 m resolution, denoted as $\hat{X}_3(s, t_2, LST, r_3)$, where $r_3 = 10 \text{ m}$. To achieve this, we rely on the Terra MODIS LST at the same date $X_1(s, t_2, LST, r_1)$ with $r_1 = 1 \text{ km}$, as well as a prior reference date $t_1 < t_2$ where all RS satellites provide valid LST observations over the geographic region s . At t_1 , we construct a prior triple T_1 composed of:

- Sentinel-2 spectral indices ($r_3 = 10 \text{ m}$): $X_3(s, t_1, NDVI, r_3)$, $X_3(s, t_1, NDWI, r_3)$, and $X_3(s, t_1, NDBI, r_3)$.
- Landsat 8 spectral indices and LST ($r_2 = 30 \text{ m}$): $X_2(s, t_1, NDVI, r_2)$, $X_2(s, t_1, NDWI, r_2)$, $X_2(s, t_1, NDBI, r_2)$, and $X_2(s, t_1, LST, r_2)$.
- Terra MODIS LST ($r_1 = 1 \text{ km}$): $X_1(s, t_1, LST, r_1)$.

Here, NDVI, NDWI, and NDBI characterize vegetation, water, and built-up surfaces, respectively. Their formulations are summarized in Table II. These indices are widely used in LST studies due to their strong correlations with surface thermal behavior [45], [46]. We intentionally limit the indices to these three to maintain compactness and prevent redundancy.

Thus, given the prior triple T_1 and the Terra MODIS LST at t_2 , the STF task is formulated as learning a DL network f , parameterized by \mathbf{W} , to estimate the target 10 m LST, as defined in Equation 2. Note that WGAST relies solely on a previous date t_1 , and thus eliminates the need to wait for a future overlapping period.

$$\hat{X}_3(s, t_2, LST, r_3) = f(T_1, X_1(s, t_2, LST, r_1) | \mathbf{W}). \quad (2)$$

TABLE II
FORMULATIONS OF SPECTRAL INDICES FOR LANDSAT 8 AND SENTINEL-2. NIR: NEAR-INFRARED, SWIR: SHORTWAVE INFRARED, RED AND GREEN REFER TO VISIBLE BANDS. B_i DENOTES THE i -TH BAND OF THE CORRESPONDING SATELLITE SENSOR.

Index	Equation	Landsat 8	Sentinel-2
NDVI	NIR-Red	$B5-B4$	$B8-B4$
	NIR+Red	$B5+B4$	$B8+B4$
	SWIR-NIR	$B6-B5$	$B11-B8$
NDBI	SWIR+NIR	$B6+B5$	$B11+B8$
	Green-NIR	$B3-B5$	$B3-B8$
NDWI	Green+NIR	$B3+B5$	$B3+B8$

III. METHODOLOGY

This section first reviews GANs and conditional GANs (cGANs), which form the basis of our approach. We then present the overall WGAST architecture and describe its main components: the generator, the weakly supervised learning strategy, the discriminator, and the loss functions.

A. Generative Adversarial Networks

GANs, introduced by [32], are a powerful class of deep generative models. They are based on a two-player adversarial game between two networks, a generator G and a discriminator D [47]. The generator synthesizes realistic samples that mimic the distribution of real data $x \sim p_{\text{data}}$, while the discriminator distinguishes them from generated samples $G(z)$, where $z \sim p_z$ is drawn from a latent prior distribution [48].

The discriminator outputs a probability map that indicates the likelihood that each input pixel is real or generated. It is optimized to maximize its classification accuracy, as expressed in Equation 3.

$$\mathcal{L}_D = \max_D \mathbb{E}_{x \sim p_{\text{data}}} [\log D(x)] + \mathbb{E}_{z \sim p_z} [\log(1 - D(G(z)))] \quad (3)$$

In contrast, the generator attempts to produce samples that fool the discriminator into classifying them as real. Its loss is defined in Equation 4.

$$\mathcal{L}^{(G)} = \min [\log D(x) + \log(1 - D(G(z)))] \quad (4)$$

The overall GAN training can be formulated as a minimax optimization problem as expressed in Equation 5.

$$L = \min_G \max_D [\log D(x) + \log(1 - D(G(z)))] \quad (5)$$

During training, the generator and discriminator engage in an adversarial interplay, as the generator improves at producing convincing samples, the discriminator enhances its ability to distinguish them from real ones. This iterative process drives both models to co-evolve and become increasingly

competent. Theoretically, this dynamic converges to a Nash equilibrium [49], where the generator has learned the true data distribution so well that the discriminator can no longer reliably differentiate real from fake.

cGANs [50] extend standard GANs by providing additional input information, called the condition. This can be class labels, images, or other contextual data, which guide the generator to produce outputs dependent on it. As a result, cGANs enable more targeted and context-aware generation, valuable when outputs must align with a specific input modality.

B. Overall Architecture

The overall architecture of WGAST is shown in Fig.2. It is based on a cGAN, where generation is explicitly conditioned on the Terra MODIS LST observation at the target time. The goal is to estimate the LST at 10 m resolution for a given region s at target time t_2 . The generated output is denoted as $\tilde{X}_3(s, t_2, LST, r_3)$, where $r_3 = 10$ m. We chose a cGAN over other generative models for three reasons [51]. First, overlapping triples are limited, and cGANs can learn effectively from smaller datasets, whereas diffusion models usually require very large ones. Second, adversarial training ensures realistic, high-resolution LST patterns and enforces spatial consistency. Third, inference is efficient. Unlike diffusion models, which require iterative denoising, cGAN generates 10 m LST in a single forward pass, making it suitable for large-scale regions.

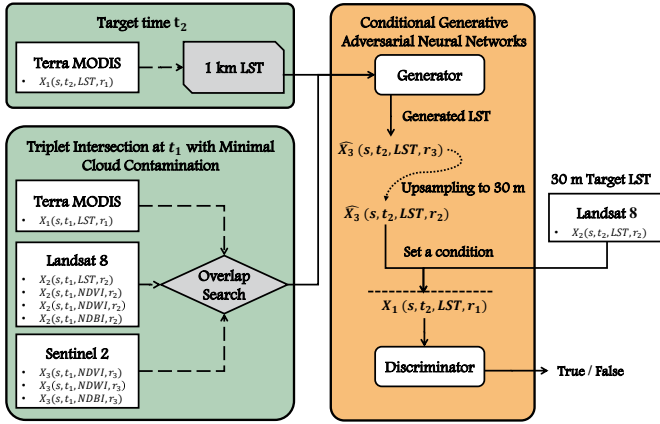


Fig. 2. Overview of the WGAST framework. WGAST consists of a generator that fuses data from Terra MODIS ($r_1 = 1$ km), Landsat 8 ($r_2 = 30$ m), and Sentinel-2 ($r_3 = 10$ m) to produce a high-resolution LST estimate at 10 m. A discriminator ensures the quality of the generated LST by comparing it with the reference Landsat 8 LST at 30 m resolution.

WGAST begins by identifying the overlapping timestep between the three RS satellites, as discussed in Section II, to extract the triple T_1 . This triple, along with the Terra MODIS LST observation at the target time t_2 , $X_1(s, t_2, LST, r_1)$ where $r_1 = 1$ km, is used as input to the generator module. The generator is designed to capture relevant spatio-spectral and spatio-temporal features from the inputs to produce a fine-resolution LST observation at 10 m for the target date t_2 . Since no ground-truth LST data at 10 m resolution are available, we adopt a weakly-supervised strategy motivated by physical principles. Specifically, the generated LST is averaged using a 3×3 window to approximate a 30 m resolution. This

output is then fed to the discriminator, which receives both the downsampled generated LST and a reference Landsat 8 30 m LST, each conditioned on the Terra MODIS LST observation at time t_2 .

C. Generator

The WGAST generator, as depicted in Fig.3, consists of four stages: *feature extraction*, *feature fusion*, *LST reconstruction*, and *noise suppression*.

1) *Feature extraction*: This stage uses a set of encoders composed of convolutional layers with downsampling and residual blocks to capture spatial and temporal features. Batch Normalization layers are omitted in the residual blocks, as they degrade GAN image synthesis quality [52]. The extracted features are encoded into compact latent representations that enable the fusion stage to operate on the most informative abstractions. Specifically, five encoders produce multi-level feature sets as follows:

- *Encoder 1*: 10 m Sentinel-2 indices (NDVI, NDBI, NDWI) features at t_1 , denoted as $\mathbf{L}_{r_3}^1 = \{\mathbf{L}_{r_3,i}^1\}_{i=0}^N$.
- *Encoder 2*: 30 m Landsat 8 indices (NDVI, NDBI, NDWI) features at t_1 , denoted as $\mathbf{L}_{r_2}^1 = \{\mathbf{L}_{r_2,i}^1\}_{i=0}^N$.
- *Encoder 3*: 30 m Landsat 8 LST features at t_1 , denoted as $\mathbf{F}_{r_2}^1 = \{\mathbf{F}_{r_2,i}^1\}_{i=0}^N$.
- *Encoder 4*: 1 km Terra MODIS LST features at t_1 , denoted as $\mathbf{F}_{r_1}^1 = \{\mathbf{F}_{r_1,i}^1\}_{i=0}^N$.
- *Encoder 5*: 1 km Terra MODIS LST features at t_2 , denoted as $\mathbf{F}_{r_1}^2 = \{\mathbf{F}_{r_1,i}^2\}_{i=0}^N$.

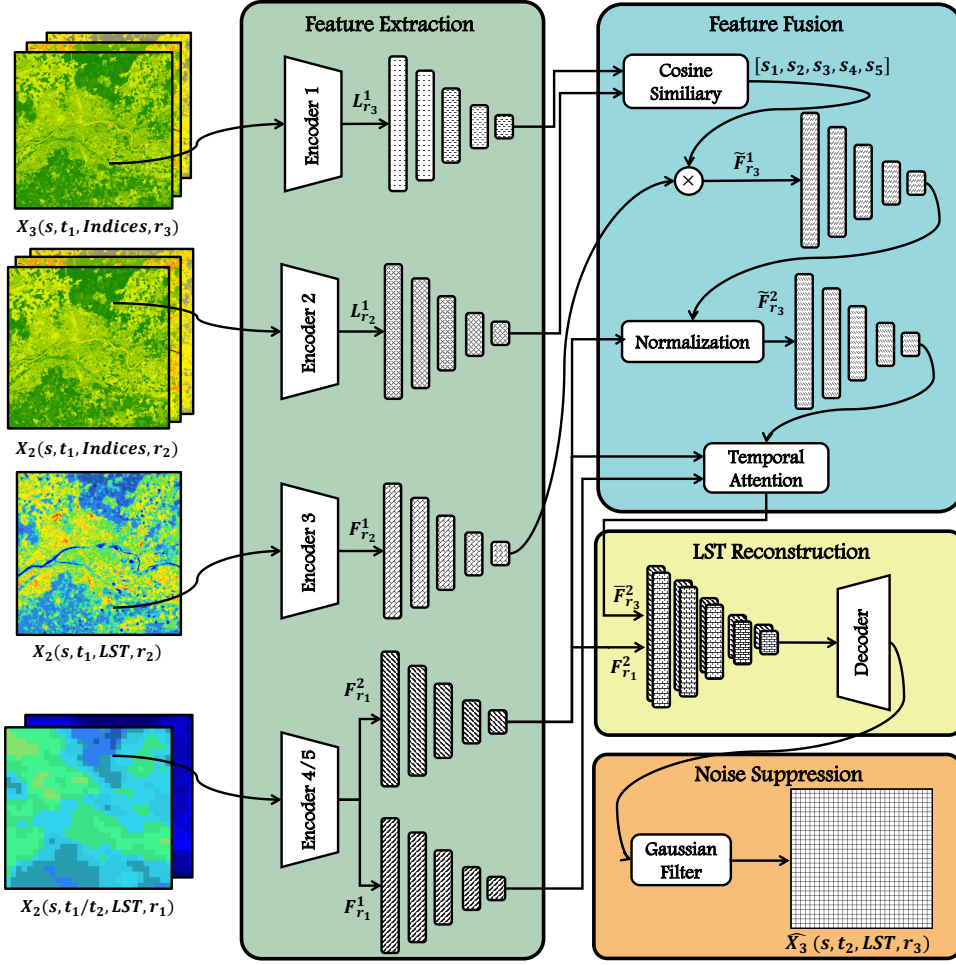
Here, N denotes the number of multi-level features produced by each encoder. Each feature group captures spatial or temporal characteristics at different levels of abstraction. Based on empirical evaluation, we fixed $N = 5$ to ensure a good balance between feature richness and computational efficiency.

2) *Feature fusion*: Feature fusion involves three operations: *cosine similarity*, *normalization*, and *temporal attention*. The *cosine similarity* between two feature vectors $\mathbf{u}, \mathbf{v} \in \mathbb{R}^C$, where C denotes the number of feature channels, is computed as in Equation 6.

$$\cos(\mathbf{u}, \mathbf{v}) = \frac{\mathbf{u} \cdot \mathbf{v}}{\|\mathbf{u}\|_2 \|\mathbf{v}\|_2} \quad (6)$$

Where $\|\cdot\|_2$ denotes the L2 norm. This metric measures the cosine of the angle between two vectors, ranging from -1 (opposite) to 1 (aligned), with 0 indicating no similarity. In image feature maps, it is applied element-wise across the feature space. In WGAST, The goal is to compute a similarity score between the multi-level features of Sentinel-2 indices at t_1 , $\mathbf{L}_{r_3}^1$, and the multi-level features of Landsat 8 indices at the same time, $\mathbf{L}_{r_2}^1$. This score is then used to spatially refine the Landsat 8 LST features $\mathbf{F}_{r_2}^1$, to produce a 10 m features approximation of LST at t_1 , denoted as $\tilde{\mathbf{F}}_{r_3}^1 = \{\tilde{\mathbf{F}}_{r_3,i}^1\}_{i=0}^N$, where each level i is computed as in Equation 7.

$$\tilde{\mathbf{F}}_{r_3,i}^1 = \mathbf{F}_{r_2,i}^1 \odot \cos(\mathbf{L}_{r_2,i}^1, \mathbf{L}_{r_3,i}^1) \quad (7)$$


Notations :

- t_1, t_2 : reference and target dates, respectively
- X_1, X_2, X_3 : Terra MODIS, Landsat 8, and Sentinel-2
- $L_{r_3}^1$: spectral index features (NDVI, NDBI, NDWI) at spatial resolution r_3 and date t_1
- $F_{r_3}^1, F_{r_3}^2$: LST features at spatial resolution r_3 at t_1 and t_2 respectively
- s_i : cosine similarity score between feature pairs level i
- $\tilde{F}_{r_3}^1, \tilde{F}_{r_3}^2, \tilde{F}_{r_3}^3$: processed LST features at spatial resolution r_3 :
 - $\tilde{F}_{r_3}^1$: after cosine similarity (at t_1)
 - $\tilde{F}_{r_3}^2$: after normalization (at t_2)
 - $\tilde{F}_{r_3}^3$: after temporal attention (at t_2)

Fig. 3. Overall architecture of the WGAST generator composed of four main stages: *feature extraction*, *feature fusion*, *LST reconstruction*, and *noise suppression*, with $r_1 = 1$ km, $r_2 = 30$ m, and $r_3 = 10$ m.

Unlike linear models that assume a global linear relationship between indices and LST values, cosine similarity is a non-linear measure that captures local, level-wise structural correspondences between feature maps at different resolutions. This allows the refinement process to emphasize features that are both semantically meaningful and spatially aligned, leading to more accurate and context-aware estimations.

In the second operation, we use *Adaptive Instance Normalization* (AdaIN) [53] to harmonize the distributions between spatially detailed and temporally consistent features. Specifically, we align the 10 m LST features extracted from the pervious step $\tilde{F}_{r_3}^1$ with the style statistics of Terra MODIS LST features at time t_2 , $F_{r_1}^2$. AdaIN proceeds in two steps: each level i of $\tilde{F}_{r_3}^1$ is first normalized by removing its mean and standard deviation, then rescaled and shifted using the statistics of the style features $F_{r_1}^2$. This is expressed in Equation 8.

$$\tilde{F}_{r_3}^2 = \text{AdaIN}(\tilde{F}_{r_3}^1, F_{r_1}^2, i) = \sigma(F_{r_1}^2, i) \cdot \frac{\tilde{F}_{r_3}^1 - \mu(\tilde{F}_{r_3}^1)}{\sigma(\tilde{F}_{r_3}^1)} + \mu(F_{r_1}^2, i) \quad (8)$$

Where $\mu(\cdot)$ and $\sigma(\cdot)$ denote the mean and standard deviation of feature map level i .

The final step, *temporal attention*, models how temporal feature variations, $F_{r_1}^1$ and $F_{r_1}^2$, affect spatial feature structure. Its goal is to integrate this temporal information into the AdaIN-normalized spatial features $\tilde{F}_{r_3}^2$. This is achieved through a spatially adaptive attention mechanism that estimates a set of attention weights $\theta = \{\theta_i\}_{i=0}^N$, where each $\theta_i \in [0, 1]$ represents the relative importance of temporal features at level i . These weights are learned dynamically during training and control the influence of temporal variations in synthesizing the final 10 m feature representation at time t_2 . Specifically, a 1×1 convolution with batch normalization projects the Terra MODIS LST features at t_1 and t_2 into a compact and discriminative space. Their difference captures temporal variations, which is processed through another 1×1 convolution and a sigmoid activation to generate an attention mask. The mask then adaptively fuses the normalized spatial features with temporal features at t_2 . The full procedure is detailed in Algorithm 1.

3) *LST Reconstruction*: The reconstruction stage mirrors the encoder through a symmetric U-Net-like architecture composed of upsampling layers, transposed convolutions, and residual blocks to reconstruct the 10 m LST at time t_2 . It

Algorithm 1: Temporal attention-based fusion

Input: $F_{r_1}^1$: Terra MODIS LST features at time t_1
 $F_{r_1}^2$: Terra MODIS LST features at time t_2
 $\tilde{F}_{r_3}^2$: Normalized spatial features at time t_2
Output: $\overline{F}_{r_3}^2$: 10 m LST features at time t_2
 $\overline{F}_{r_3}^2 \leftarrow [\cdot] \cdot N$
foreach $i = 1, \dots, N$ **do**
 $F1 \leftarrow \text{Conv1x1_BN}(F_{r_1}^1[i])$
 $F2 \leftarrow \text{Conv1x1_BN}(F_{r_1}^2[i])$
 $\Delta F \leftarrow F1 - F2$
 $\theta_i \leftarrow \text{Sigmoid}(\text{Conv1x1_BN}(\Delta F))$
 $\overline{F}_{r_3}^2[i] \leftarrow F_{r_1}^2[i] \cdot \theta_i + \tilde{F}_{r_3}^2[i] \cdot (1 - \theta_i)$
return $\overline{F}_{r_3}^2$

takes as input the temporally attended spatial features $\overline{F}_{r_3}^2$ and the original Terra MODIS LST features $F_{r_1}^2$, concatenated along the channel dimension. Reintroducing $F_{r_1}^2$ at this stage preserves large-scale temperature patterns that may have been weakened during earlier fusion and normalization. The combined features are decoded and progressively refined to produce the final 10 m LST output, denoted as $\overline{X}_3(s, t_2, LST, r_3)$.

4) *Noise Suppression:* The *noise suppression* module reduces high-frequency artifacts present in the reconstructed LST $\overline{X}_3(s, t_2, LST, r_3)$, to produce a spatially and temporally coherent result, $\hat{X}_3(s, t_2, LST, r_3)$. This step is essential since LST fields in geophysical contexts exhibit smooth, spatially continuous patterns driven by heat diffusion rather than abrupt variations. However, deep generators with multiple upsampling layers and skip connections can unintentionally amplify pixel-level noise and produce unrealistic high-frequency textures that deviate from the expected physical smoothness of LST. To address this, we apply a Gaussian filter to smooth local fluctuations while preserving spatial structure and physical coherence. The Gaussian kernel is defined in Equation 9.

$$G(x, y; \sigma) = \frac{1}{2\pi\sigma^2} \exp\left(-\frac{x^2 + y^2}{2\sigma^2}\right) \quad (9)$$

where σ controls the smoothing degree. A higher σ produces stronger smoothing. In WGAST, σ is fixed to 1.

The noise suppression is then implemented via depthwise convolution of the predicted LST with the Gaussian kernel, as expressed in Equation 10.

$$\hat{X}_3(s, t_2, LST, r_3) = \text{Conv2D}(\overline{X}_3(s, t_2, LST, r_3), G(x, y; \tau)) \quad (10)$$

where $G(x, y; \tau)$ is the two-dimensional Gaussian kernel defined in Equation 9, and the kernel size is $k = 2 \cdot \lceil 3\sigma \rceil + 1$. Reflective padding is used to reduce boundary artifacts.

D. Weakly Supervised Learning

In the absence of ground-truth LST data at 10 m resolution, we employ a weakly supervised learning strategy guided by physical principles. Prior studies have shown that coarse-resolution LST can be approximated by local averages of

finer-resolution values [54]. Under the assumption of limited thermal variability within small areas, a 30 m LST value can thus be estimated by averaging a 3×3 neighborhood of 10 m pixels. This corresponds to the inexact supervision paradigm of weakly supervised learning, where coarse-scale data are used to train models that predict fine-scale outputs [55].

Based on this principle, we apply a 3×3 average pooling operation to the generator's output $\hat{X}_3(s, t_2, LST, r_3)$ to obtain a 30 m estimate, as expressed in Equation 11. This upsampled output is compared to the corresponding Landsat 8 LST observation at t_2 , denoted $X_2(s, t_2, LST, r_2)$. The Landsat 8 LST is used only during training. This enables the model to depend solely on temporally frequent Terra MODIS inputs at inference time, thus preserving daily temporal coverage.

$$\hat{X}_3(s, t_2, LST, r_2)(m, n) = \frac{1}{9} \sum_{i=0}^2 \sum_{j=0}^2 \hat{X}_3(s, t_2, LST, r_3)(3m + i, 3n + j) \quad (11)$$

E. Discriminator

WGAST discriminator is built upon the PatchGAN architecture [32] (Fig.4). Unlike standard GANs that classify entire images as real or fake, here it discriminates between observed and fused LST. The discriminator takes as input the fused LST conditioned on the corresponding Terra MODIS LST $X_1(s, t_2, LST, r_1)$, which provides reliable thermal context at 1 km resolution. This conditioning enables the model to verify whether the target LST exhibits physically consistent temperature patterns with the Terra MODIS data. The final layer applies a softmax function to output probabilities, where higher values indicate greater confidence that a patch is real. During training, the discriminator is expected to output probabilities close to 1 for real Landsat 8 LST samples $X_2(s, t_2, LST, r_2)$ and close to 0 for fused outputs $\hat{X}_3(s, t_2, LST, r_2)$, both conditioned on the Terra MODIS input.

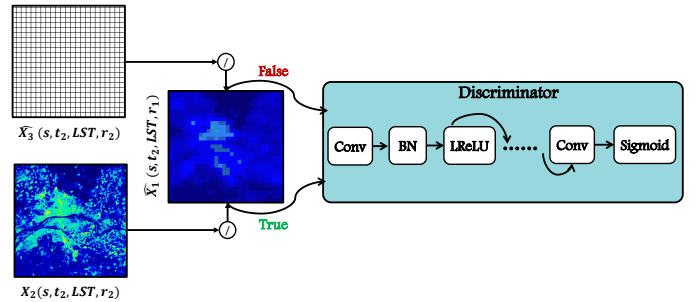


Fig. 4. WGAST discriminator based on the PatchGAN architecture.

F. Loss Functions

1) *Discriminator Loss:* The discriminator is trained to distinguish between real LST observations and fused LST outputs generated by the model. Its objective function, denoted as \mathcal{L}_D , is defined in Equation 12. For brevity, we use the notation $\hat{X}_3(LST, r_2)$ to represent $\hat{X}_3(s, t_2, LST, r_2)$, and apply the same simplification to X_2 and X_1 .

$$\mathcal{L}_D = \frac{1}{2} \mathbb{E}_{\hat{X}_3, X_1} \left[\left(D \left(\hat{X}_3(LST, r_2) \mid X_1(LST, r_1) \right) \right)^2 \right] + \frac{1}{2} \mathbb{E}_{X_2, X_1} \left[\left(D \left(X_2(LST, r_2) \mid X_1(LST, r_1) \right) - 1 \right)^2 \right] \quad (12)$$

Where $D(\cdot)$ denotes the discriminator. The loss adopts the least-squares GAN formulation [56], which penalizes the discriminator for assigning values far from 0 for fused generated LST and far from 1 for real LST, thereby stabilizing training and mitigating vanishing gradients. The expectations \mathbb{E} denote averages taken over training samples.

2) *Generator Loss*: The generator loss, denoted by \mathcal{L}_G , combines adversarial feedback with several image-based losses to ensure both realism and fidelity in the fused output. The full loss formulation is given in Equation 13.

$$\begin{aligned} \mathcal{L}_G = & \underbrace{\alpha \mathbb{E}_{\hat{X}_3, X_1} \left[\left(D \left(\hat{X}_3(LST, r_2) \mid X_1(LST, r_1) \right) - 1 \right)^2 \right]}_{\mathcal{L}_{GAN}} \\ & + \beta \underbrace{\frac{1}{K} \sum_{k=1}^K \left| \hat{X}_3(LST, r_2) - X_2(LST, r_2) \right|}_{\mathcal{L}_{content}} \\ & + \gamma \underbrace{\left(1 - \frac{\langle \hat{X}_3(LST, r_2), X_2(LST, r_2) \rangle}{\|\hat{X}_3(LST, r_2)\|_2 \|X_2(LST, r_2)\|_2} \right)}_{\mathcal{L}_{spectrum}} \\ & + \delta \underbrace{\left(1 - \text{MS-SSIM} \left(\hat{X}_3(LST, r_2), X_2(LST, r_2) \right) \right)}_{\mathcal{L}_{vision}} \end{aligned} \quad (13)$$

Here, the adversarial loss \mathcal{L}_{GAN} encourages the generator to produce fused LST outputs $\hat{X}_3(s, t_2, LST, r_2)$ that the discriminator cannot distinguish from real LST observations, conditioned on the corresponding Terra MODIS input $X_1(s, t_2, LST, r_1)$. The content loss $\mathcal{L}_{content}$ is computed as the pixel-wise L1 distance, which promotes numerical consistency with real LST values. The spectrum loss $\mathcal{L}_{spectrum}$, defined as one minus the cosine similarity, preserves the overall spatial variability and temperature distribution. Finally, the vision loss \mathcal{L}_{vision} , derived from the Multiscale Structural Similarity Index (MS-SSIM), captures perceptual and structural coherence across multiple spatial scales. The hyperparameters α , β , γ , and δ control the relative importance of each loss component in the overall generator loss function. In WGAST, we fixed $\alpha = 10^{-2}$, $\beta = 1$, $\gamma = 1$, and $\delta = 1$.

IV. EXPERIMENTAL RESULTS

A. Region of Interest

The region of interest (ROI) is located within Orléans Métropole, France. As shown in Fig.5(a1), it spans latitudes $47^\circ 50' 41.77''\text{N}$ to $47^\circ 54' 1.74''\text{N}$ and longitudes $1^\circ 50' 6.98''\text{E}$ to $1^\circ 59' 36.36''\text{E}$, covering approximately 114km^2 . The Loire River, France's longest, traverses the ROI and plays a significant geographical and thermal role (Fig.5(a2)). The area features a diverse land cover mosaic, including dense urban

areas, water bodies, forests, industrial zones, and croplands (Fig.5(b1)–(b5)). Such heterogeneity introduces a wide range of radiative, thermal, and textural surface characteristics. This makes it a suitable benchmark for evaluating WGAST's spatial adaptability and generalization, particularly in urban settings where LST varies sharply over short distances.

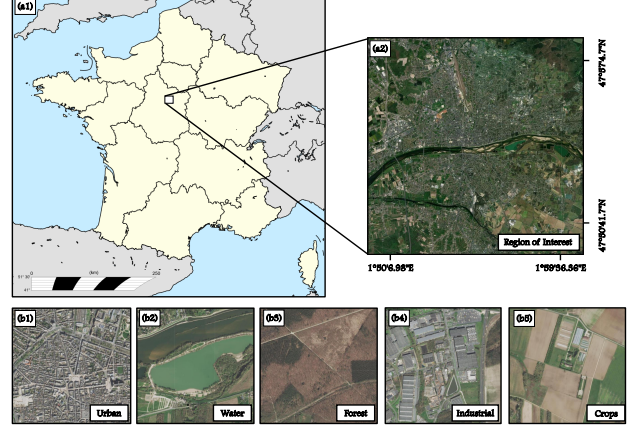


Fig. 5. Geographic overview of the ROI. (a1) Position of the ROI within France. (a2) High-resolution satellite image of the ROI. (b1)–(b5) Representative examples of key land cover categories observed in the ROI: urban, water, forest, industrial, and agricultural zones.

B. Datasets

1) *Satellite Data*: The RS satellite data X_1 , X_2 , and X_3 were obtained from the Google Earth Engine (GEE) platform [57]. Terra MODIS data were accessed from the MOD11A1 (Collection 6.1) daily 1 km product, which provides atmospherically corrected LST values via the LST_Day_1km band, with a reported RMSE within 2°C [58]. Landsat 8 data were obtained from the USGS Level-2 Collection 2 Tier 1 dataset, with LST derived from the ST_B10 thermal band and estimated using a single-channel algorithm, with an accuracy of approximately 1.5°C [59]. NDVI, NDWI, and NDBI were computed from SR bands SR_B3 , SR_B4 , SR_B5 , and SR_B6 . Sentinel-2 imagery was collected from the Harmonized MSI Level-2A collection, with NDVI, NDWI, and NDBI computed from SR bands $B2$, $B3$, $B4$, $B8$, and $B11$. Table III lists the 11 selected samples, each consisting of a reference date t_1 and target date t_2 . At t_1 , Terra MODIS, Landsat 8, and Sentinel-2 acquisitions overlapped spatially and temporally. At t_2 , WGAST uses only Terra MODIS LST for input, with Landsat 8 reserved for evaluation. For example, to predict 10 m LST on 23 Feb 2018 (t_2), WGAST takes the Terra MODIS LST at t_2 and the triple T_1 from 09 Apr 2017 (t_1) to generate a fused LST, which is then upsampled and compared with Landsat 8 acquired on t_2 . The satellite overpasses are closely aligned, with a maximum time difference of about 1 h 15 min, occurring between 10:00 and 12:00 local time. This mid-morning window ensures stable surface and atmospheric conditions, and thus minimizes variations in LST and SR, and reinforces the suitability of the fusion process. Resolutions are 1200×1200 pixels for Sentinel-2 and 400×400 for Landsat 8, with all samples having cloud

TABLE III
SUMMARY OF THE 11 SELECTED SAMPLES, EACH WITH A REFERENCE (t_1) AND TARGET (t_2) TIME.

Sample No.	Reference Date t_1				Target Date t_2		
	Date	Terra MODIS	Landsat 8	Sentinel-2	Date	Terra MODIS	Landsat 8
1	09 Apr 2017	11:54	10:40	11:05	23 Feb 2018	11:54	10:40
2	21 Oct 2018	11:54	10:41	11:06	26 Feb 2019	11:54	10:40
3	06 Sep 2019	11:54	10:41	11:07	01 Apr 2020	11:54	10:40
4	22 Jul 2020	11:54	10:41	11:07	07 Aug 2020	11:54	10:41
5	06 Mar 2022	11:48	10:41	10:57	22 Mar 2022	11:48	10:41
6	13 Aug 2022	11:42	10:41	10:57	29 Aug 2022	11:42	10:41
7	28 May 2023	11:10	10:40	11:07	13 Jun 2023	10:36	10:40
8	12 Apr 2024	10:35	10:40	11:07	19 Sep 2024	10:00	10:41
9	19 Sep 2024	10:00	10:41	11:07	05 Oct 2024	10:48	10:41
10	19 Sep 2024	10:00	10:41	11:07	21 Oct 2024	10:06	10:41
11	19 Sep 2024	10:00	10:41	11:07	01 May 2025	09:30	10:40

contamination below 20%. Missing pixels due to clouds or technical issues were filled via adaptive spatial interpolation using a 3×3 local mean window, expanded progressively by steps of 2 until at least one valid neighbor was included.

The first 7 samples were used for training, with patch sizes of 96×96 and a stride of 24 for Sentinel-2 (32×32 and a stride of 8 for Landsat 8), yielding 15,463 training patches. The remaining 4 samples were reserved for testing. To prevent temporal leakage, reference dates t_1 of a sample were not allowed to coincide with target dates t_2 of other training samples. Testing samples were independent, thus overlap was allowed. WGAST was trained with a learning rate of 2×10^{-4} and batch size of 32 on an NVIDIA RTX A6000 GPU.

2) *In-situ Measurement*: To validate WGAST under real-world conditions, we used a network of 33 near-ground sensors distributed across the ROI, each measuring near-surface air temperature (T_a) at a height of 2 m following standard meteorological protocols. The validation period extended from 1 April to 30 May 2025, during which 25 cloud-free Terra MODIS LST images were acquired. Accordingly, WGAST generated 25 cloud-free LST maps at 10 m resolution for the same dates. Fig.6 shows the spatial distribution of the sensors. During this period, only two Landsat 8 LST acquisitions (1 May and 17 May 2025) were available, both partially affected by clouds. Moreover, no usable Landsat 8 data were available in April due to persistent cloud cover and technical issues. In contrast, WGAST produced 25 complete LST observations over the same timeframe.

Although T_a and LST represent distinct physical variables, they exhibit strong radiative coupling under clear-sky daytime conditions. This relationship makes T_a a reliable proxy for indirectly evaluating the consistency and physical realism of WGAST’s fused LST outputs. Additionally, field observations indicate that T_a remains relatively stable within a 10 m spatial window, making it comparable to the 10 m WGAST-derived LST maps. Thus, for each sensor location, we extracted its exact geographic coordinates from the fused LST maps and assigned the corresponding $10 \text{ m} \times 10 \text{ m}$ pixel value as the representative LST. This produced a spatially aligned dataset of paired T_a and LST values.



Fig. 6. Spatial distribution of the in-situ near-ground sensors across the ROI. The central map shows all sensor locations (orange dots), while the zoomed-in insets highlight the detailed placement of selected sensors (Sensors 03, 06, 13, 17, 21, and 31) within their immediate surroundings.

C. Quantitative Assessment

1) *Convergence Analysis*: Fig.7 shows the training evolution of the generator and discriminator losses during adversarial training. The generator loss starts relatively high at ~ 2.53 , reflecting its initial inability to capture complex spatio-temporal relationships. As training progresses and the generator produces more realistic fused LST, the loss decreases steadily to ~ 0.58 . Conversely, the discriminator begins with a low loss of ~ 0.07 , indicating that distinguishing real from generated LST is initially easy due to the low quality of fused outputs. As the generator improves, the discriminator’s task becomes more difficult, leading to a gradual increase in its loss. This opposing behavior illustrates the adversarial dynamics of cGANs. Eventually, both losses stabilize near a Nash equilibrium, which indicates convergence.

2) *Model Performance Analysis*: WGAST was evaluated over four dates using six established metrics. Two are error metrics: Root Mean Square Error (RMSE) and Error Relative Global Dimensionless Synthesis (ERGAS), which quantify pixel-wise discrepancies between the generated and reference LST. The remaining four are quality metrics: Structural Similarity Index Measure (SSIM), Peak Signal-to-Noise Ratio (PSNR), Spectral Angle Mapper (SAM), and Correlation Coefficient (CC), which assess perceptual, spectral, and structural

TABLE IV
 QUANTITATIVE COMPARISON OF WGAST AGAINST BICUBIC, TEN-ST [42], GAN-10, AE-10 AND FUSETEN [44] OVER FOUR DATES.

Metric	19 Sep 2024						05 Oct 2024					
	BicubicI	Ten-ST	GAN-10	AE-10	FuseTen	WGAST	BicubicI	Ten-ST	GAN-10	AE-10	FuseTen	WGAST
RMSE (↓)	3.637	3.934	4.589	3.396	3.220	2.619	2.451	2.583	2.008	1.623	1.050	1.386
SSIM (↑)	0.640	0.526	0.365	0.424	0.798	0.814	0.666	0.621	0.491	0.553	0.863	0.912
PSNR (↑)	15.357	14.503	13.826	15.953	18.552	21.399	17.765	17.310	19.497	21.348	25.657	24.990
SAM (↓)	4.841	6.168	6.143	5.509	3.865	5.428	3.162	4.677	6.158	4.658	2.823	3.604
CC (↑)	0.572	-0.025	0.431	0.437	0.814	0.747	0.571	0.113	0.664	0.663	0.901	0.860
ERGAS (↓)	4.595	4.983	5.798	4.290	3.944	3.309	4.190	4.447	3.433	2.774	1.795	2.293
	21 Oct 2024						01 May 2025					
RMSE (↓)	2.150	2.342	2.676	2.294	1.905	1.487	4.724	5.340	6.198	3.875	3.234	2.312
SSIM (↑)	0.770	0.837	0.414	0.519	0.867	0.895	0.538	0.707	0.486	0.582	0.790	0.841
PSNR (↑)	18.450	24.592	16.582	17.888	21.748	25.322	16.186	21.281	13.827	17.906	19.476	23.105
SAM (↓)	3.930	4.689	4.690	3.813	3.033	3.673	5.823	7.625	5.782	5.739	3.918	3.888
CC (↑)	0.494	0.120	0.546	0.579	0.896	0.887	0.538	0.095	0.556	0.580	0.840	0.826
ERGAS (↓)	3.315	3.610	4.126	3.537	2.937	2.293	4.819	5.515	6.323	3.953	3.300	2.358

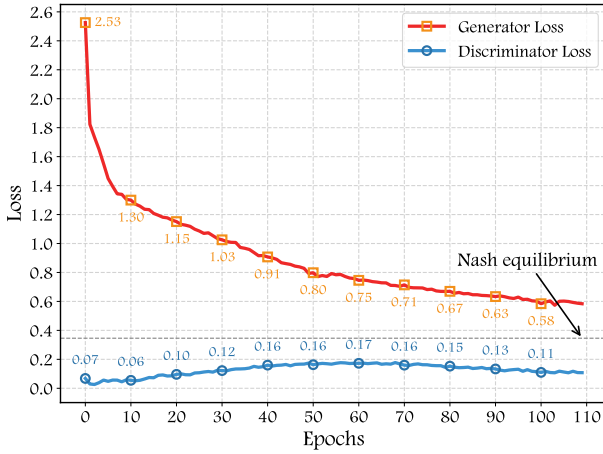


Fig. 7. Evolution of generator and discriminator losses during WGAST training. The generator loss decreases as it learns to produce more realistic fused LST, while the discriminator loss increases as its task becomes more challenging. Both losses eventually stabilize.

fidelity. For evaluation, predicted 10 m LSTs were averaged within a 3×3 window to match the 30 m resolution and validated against Landsat 8 LST. Each test image was divided into overlapping patches, and WGAST predicted LST for each patch independently. Overlapping predictions were then merged using soft border weighting to reduce boundary artifacts and ensure smooth reconstruction. We compared WGAST against five baselines. The first three are BicubicI, Ten-ST [42], and FuseTen [44]. BicubicI performs bicubic interpolation to upscale Terra MODIS LST to Sentinel-2 resolution, and thus produces daily LST at 10 m. Ten-ST assumes a linear relationship and applies robust least-squares fusion of Terra MODIS and Sentinel-2 data to generate daily 10 m LST. FuseTen employs a hybrid cGAN model, with a generator integrating a linear regression component. As fully DL-based methods for daily 10 m LST estimation are currently unavailable, we introduce two additional baselines, GAN-10 and AE-10. These first estimate daily 30 m LST using a

GAN [36] or AutoEncoder [60], then downsample to 10 m using linear regression guided by Sentinel-2 spectral indices from the prior date t_1 .

On 19 Sep 2024, WGAST outperforms most competing methods, except for SAM and CC. Compared to FuseTen, it reduces RMSE by 18.66%, increases SSIM by 2.01%, improves PSNR by 15.35%, and decreases ERGAS by 16.10%, indicating more accurate pixel-wise LST estimates and enhanced spatial and spectral fidelity. The slightly higher SAM and marginally lower CC reflect WGAST’s emphasis on preserving local spatial details and structural sharpness, occasionally at the expense of global angular alignment. Compared to Ten-ST-GEE, WGAST achieves even larger gains, including a 33.43% RMSE reduction, 54.75% SSIM increase, 47.55% PSNR gain, and 33.60% ERGAS decrease. Relative to AE-10, RMSE drops by 22.88% and SSIM increases by 91.98%, with similar improvements across other metrics. On 05 Oct 2024, WGAST performance is comparable to FuseTen, with an RMSE of 1.386, slightly higher than FuseTen’s 1.050. Similar trends are observed for PSNR, SAM, CC, and ERGAS, while SSIM improves by 5.68%. This is likely due to the LST on this day exhibiting a linear spatio-temporal trend, which allowed FuseTen to better capture the absolute values. On 21 Oct 2024, WGAST delivers strong performance across all metrics. Compared to FuseTen, it reduces RMSE by 21.94%, increases SSIM by 3.23%, gains 16.43% in PSNR, and lowers ERGAS by 21.93%. Compared to Ten-ST-GEE, RMSE decreases by 36.51%, SSIM improves by 6.93%, PSNR increases by 2.97%, and ERGAS drops by 36.49%. Relative to AE-10, WGAST reduces RMSE by 35.18% and improves SSIM by 72.45%. On 01 May 2025, despite the large temporal gap from the reference date at t_1 (19 Sep 2024), WGAST maintains strong performance, whereas other methods show notable accuracy degradation. For instance, compared to FuseTen, WGAST achieves a 28.51% RMSE reduction and a 6.46% SSIM gain.

On average across all test dates, as shown in Table V, WGAST reduces RMSE by 17.05%, increases SSIM by 4.22%, improves PSNR by 10.98%, and lowers ERGAS by 13.76% compared to FuseTen. Relative to the best linear

method, the gains are even more pronounced, with a 39.80% RMSE reduction, 28.53% SSIM increase, 22.05% PSNR gain, and 44.41% ERGAS decrease, demonstrating consistent superiority across all evaluation metrics. These results indicate that linear baselines, hybrid models, or combinations of STF and downscaling approaches do not achieve better performance than a fully DL-based model.

TABLE V
AVERAGE QUANTITATIVE COMPARISON OF ALL METHODS.

Metric	BicubicI	Ten-ST	GAN-10	AE-10	FuseTen	WGAST
	Average					
RMSE(↓)	3.241	3.550	3.868	2.637	2.352	1.951
SSIM(↑)	0.654	0.673	0.439	0.520	0.830	0.865
PSNR(↑)	16.940	19.422	15.933	18.274	21.358	23.704
SAM(↓)	4.439	6.160	5.693	4.930	3.410	4.148
CC(↑)	0.544	0.076	0.549	0.565	0.863	0.830
ERGAS(↓)	4.073	4.645	4.920	3.639	2.994	2.582

3) *In-situ Measurement*: LST and near-surface air temperature (T_a) are fundamentally distinct physical quantities and are not directly comparable in a quantitative sense. However, under clear-sky and daytime conditions, they exhibit strong radiative coupling due to energy exchanges between the land surface and the atmosphere, which often leads to coherent spatial and temporal patterns. Accordingly, while the absolute values of fused 10 m LST and T_a may differ, their monotonic behavior is typically consistent within specific seasons [61]. In our study, we focus on the period from 01 April to 01 June 2025, which corresponds to a single season, thus allowing this assumption to be reasonably validated. Therefore, a high correlation between fused LST and T_a serves as a meaningful indicator of the physical realism and internal consistency of the predicted LST. We used the Pearson correlation coefficient (PCC) and Spearman rank correlation coefficient (SRCC) to quantify this relationship. PCC measures the strength and direction of a linear relationship between two continuous variables [62], whereas SRCC quantifies the strength and direction of a monotonic relationship [63], making it suitable for non-linear monotonic associations. Both metrics range from -1 to 1 , with values near either extreme indicating strong linear or monotonic relationships, respectively. Given two variables a and b with ranks $R(u)$ and $R(v)$, the two metrics are defined in Equation 14.

$$\text{PCC} = \frac{\text{cov}(a, b)}{\sigma_a \sigma_b}, \quad \text{SRCC} = 1 - \frac{6 \sum_{i=1}^m d_i^2}{m(m^2 - 1)} \quad (14)$$

where $\text{cov}(a, b)$ denotes the covariance between a and b , σ_a and σ_b are their standard deviations, $d_i = R(a_i) - R(b_i)$ is the difference between the ranks of the i -th values of the two variables, and m is the total number of paired data.

Table VI reports the PCC and SRCC between the WGAST’s 10 m pixel-wise LST and the corresponding near-surface air temperature (T_a) across 33 sensors. The results reveal consistently strong correlations, with PCC values ranging from 0.80 to 0.95 and SRCC values from 0.80 to 0.94. These indicate a strong and statistically meaningful relationship between the

generated LST and the near-surface T_a , which supports the physical realism and consistency of WGAST’s 10 m LST. Notably, even the lowest values exceed commonly accepted thresholds, highlighting the method’s robustness across diverse sensor locations and urban conditions. Overall, this performance underscores WGAST’s ability to reliably capture spatio-temporal variations in LST at fine spatial resolution.

TABLE VI
PCC AND SRCC BETWEEN FUSED LST AND NEAR-SURFACE AIR TEMPERATURE T_a ACROSS SENSORS

Sensor	1	2	3	4	5	6	7	8	9
PCC	0.93	0.92	0.93	0.90	0.95	0.91	0.91	0.88	0.88
SRCC	0.94	0.93	0.89	0.85	0.94	0.91	0.88	0.85	0.87

Sensor	10	11	12	13	14	15	16	17	18
PCC	0.80	0.89	0.90	0.91	0.90	0.91	0.90	0.95	0.91
SRCC	0.80	0.88	0.88	0.93	0.90	0.92	0.87	0.93	0.94

Sensor	19	20	21	22	23	24	25	26	27
PCC	0.88	0.89	0.88	0.90	0.90	0.86	0.91	0.88	0.88
SRCC	0.85	0.86	0.85	0.87	0.88	0.88	0.91	0.85	0.85

Sensor	28	29	30	31	32	33	Average
PCC	0.93	0.90	0.90	0.91	0.89	0.93	0.90
SRCC	0.91	0.85	0.87	0.87	0.91	0.93	0.89

Fig.8 displays scatter plots comparing WGAST’s 10 m fused LST with near-surface air temperature (T_a) from four randomly selected sensors during the evaluation period. These plots demonstrate a strong correspondence between LST and T_a , confirming that the fused LST product reliably captures the physical trends observed at ground level. The temporal evolution of LST and T_a shows a clear and synchronized pattern across all sensors. In nearly all cases, both LST and T_a exhibit the same monotonic behavior, with LST rising as T_a increases and following the same downward trend as T_a decreases. Even during periods of sharp thermal fluctuation, WGAST’s LST closely tracks T_a by accurately detecting peaks and valleys across diverse spatial settings. Since the selected sensors span various land cover types, these results underscore the model’s robustness and generalizability across different environments. In addition, we included the Landsat 8 LST acquisition on 01 May 2025, which was the only image partially usable with 20% cloud-free coverage. All other Landsat acquisitions during the evaluation period were either fully cloud-covered or affected by technical issues. The Landsat 8 LST values are represented as black circles in the plots. While a single Landsat observation is insufficient for full quantitative validation, it provides an independent qualitative reference, that demonstrates that the fused 10 m LST values from WGAST are broadly consistent with available satellite measurements. For instance, for sensor 15, when WGAST’s LST is below T_a , it was also the case for Landsat 8, and vice versa. Most importantly, WGAST achieves continuous LST estimates even on dates when Landsat data are missing. Overall, the analysis validates the WGAST’s ability to produce temporally coherent and physically realistic LST estimates in strong agreement with ground truth observations.

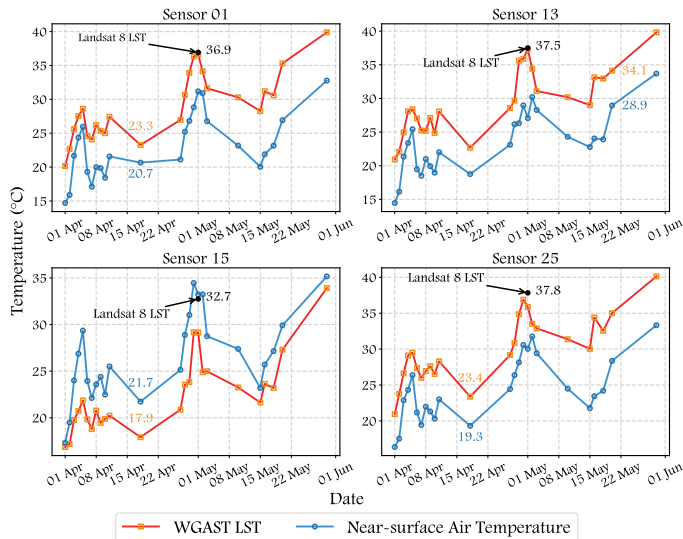


Fig. 8. Scatter plots comparing WGAST’s 10 m LST with near-surface air temperature T_a from four randomly selected sensors during the evaluation period. The plots illustrate the strong correlation and synchronized temporal patterns between the generated LST and T_a .

D. Qualitative Assessment

Fig.9 presents a qualitative comparison on 21 Oct 2024 between the 1 km Terra MODIS LST, the reference 30 m Landsat 8 LST, the 10 m LSTs generated by FuseTen and WGAST, and the corresponding high-resolution satellite image for context. Other baselines are omitted due to their inferior performance (Table V).

In Fig.9(a), WGAST produces LST distributions that closely match the Landsat 8 LST reference while preserving spatial coherence and fine thermal details. Around urban hotspots (highlighted in red), WGAST accurately captures temperature gradients and sharp river boundaries, whereas FuseTen oversmooths these transitions, losing key spatial and thermal contrasts. In semi-urban areas along the Loire and Loiret rivers, WGAST successfully reconstructs cool water surfaces and surrounding structures, including bridges and secondary channels, which are poorly defined in FuseTen. In Fig.9(b), WGAST recovers the Loire River’s cool thermal signature, its curved geometry, and surrounding landscape features. The bridge crossing the river (highlighted in red) is sharply delineated in WGAST, appearing more distinct than in both the Landsat 8 LST, where it is faint, and FuseTen, where it is nearly invisible due to oversmoothing. WGAST also captures the secondary Loiret River (highlighted in blue) with well-defined riverbanks and cooler temperatures relative to nearby urban areas. This thermal and structural contrast is hardly visible in the Landsat 8 LST. Fig.9(c) focuses on a densely forested region of the Orléans Forest, the largest forest in France. WGAST delivers a detailed reconstruction of the forest thermal structure by accurately capturing subtle intra-canopy temperature variations and preserving crisp spatial textures across the scene. The dense vegetation yields generally lower LST, a pattern faithfully reflected by WGAST. Notably, a small vegetated patch with slightly elevated LST (highlighted in

red) is correctly reproduced by WGAST in agreement with the Landsat 8 reference, whereas FuseTen assigns this patch a temperature indistinguishable from the surrounding forest and thus overlooks the anomaly. Fig.9(d) depicts a highly active industrial zone characterized by industrial facilities, dense road networks, and fragmented green spaces. WGAST accurately recovers thermal hotspots (highlighted in red) that align closely with the Landsat 8 reference by preserving the contrast between built-up and vegetated areas. In particular, a cluster of buildings showing elevated temperatures (highlighted in blue) is successfully reconstructed by WGAST with markedly higher LST than adjacent vegetated surfaces. By contrast, FuseTen excessively smooths the temperature field, merging distinct thermal patterns and obscuring land-use contrasts. It also fails to emphasize the hotspots and instead produces nearly uniform temperatures across industrial and non-industrial zones. Fig.9(e) presents the city center of Orléans Métropole, a densely built urban area traversed by the Loire River, with numerous roads and bridge-like structures. WGAST preserves urban morphology and accurately captures elevated LST in urban cores, particularly in the region highlighted in blue, consistent with the Landsat 8 reference. Linear features such as roads and bridges (highlighted in red) are sharply delineated in WGAST while maintaining thermal contrast with surrounding surfaces. The Loire River itself remains clearly defined spatially and thermally, whereas FuseTen underestimates urban LST, blurs structural details, and struggles to reproduce the river and linear features. Fig.9(f) depicts a heterogeneous urban landscape of small residential areas, streets, and vegetated spaces, intersected by the Loiret River. WGAST accurately reflects spatial diversity, separating cooler vegetated zones from warmer surfaces. In the red highlighted area, a localized hotspot is correctly reconstructed, whereas FuseTen oversmooths it. In the blue highlighted region corresponding to the river and its banks, WGAST preserves the expected thermal gradient, clearly distinguishing cooler water from warmer land, while FuseTen assigns nearly uniform temperatures that obscure this contrast.

Overall, WGAST produces more physically coherent and realistic LST than FuseTen. It preserves fine spatial structures and thermal gradients, but also generates detailed daily 10 m LST that even surpasses the 30 m Landsat reference, all derived from the coarser 1 km Terra MODIS input.

Moreover, WGAST effectively mitigates the cloud gaps commonly present in Landsat 8 LST products, as illustrated in Fig.10. This is achieved by relying solely on Terra MODIS LST at the target time, which is less affected by persistent cloud cover. Consequently, WGAST generates 10 m LST that are temporally aligned with Terra MODIS acquisitions and largely free from the missing data affecting Landsat 8. Note that the Terra MODIS input should itself be cloud-free to achieve these results.

E. Spatio-Temporal Generalization

To evaluate the spatio-temporal generalization capability of WGAST, we tested it on six additional regions with diverse geographic and climatic characteristics: Tours and

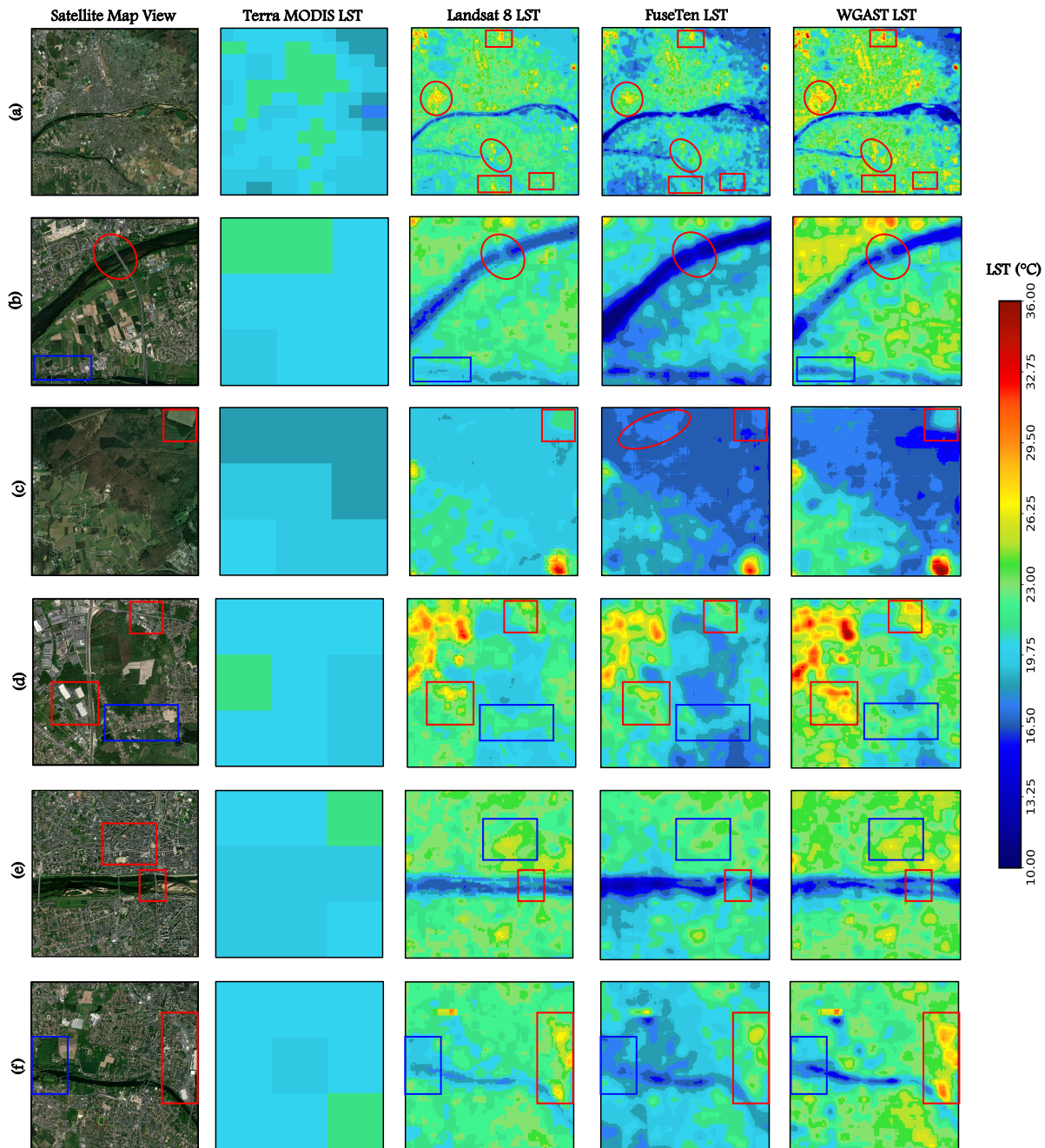


Fig. 9. Qualitative comparison of WGAST and FuseTen across six representative regions in Orléans Métropole on 21 Oct 2024: (a) the Orléans Métropole, (b) a semi-urban corridor along the Loire River, (c) the Orléans Forest, (d) a major industrial area, (e) the city center of Orléans, and (f) a mixed residential and vegetated neighborhood traversed by the Loiret River. Each row displays the high-resolution satellite view alongside the Terra MODIS LST, the Landsat 8 LST reference, and the predictions from FuseTen and WGAST.

Montpellier (France), Madrid (Spain), Rome (Italy), Cairo (Egypt), and Istanbul (Turkey). These regions span climates from temperate oceanic (Tours), Mediterranean (Montpellier, Rome), continental Mediterranean (Madrid), arid desert (Cairo), to transitional Mediterranean-continental (Istanbul). WGAST predictions were generated for 21 Oct 2024 (Tours), 01 Apr 2025 (Montpellier), 28 Mar 2025 (Madrid), 10 Jun 2025 (Rome), 23 Dec 2023 (Cairo), and 10 Apr 2025 (Istanbul), representing seasons and thermal conditions unseen during training. The ROIs used for

these tests were defined as follows. Tours extends from $47^{\circ}20'51.49''\text{N}$ to $47^{\circ}27'08.74''\text{N}$ and from $0^{\circ}36'57.71''\text{E}$ to $0^{\circ}46'13.20''\text{E}$. Montpellier spans $43^{\circ}33'27.54''\text{N}$ to $43^{\circ}39'52.00''\text{N}$ and $3^{\circ}48'09.59''\text{E}$ to $3^{\circ}56'58.73''\text{E}$. Rome covers $41^{\circ}50'11.91''\text{N}$ to $41^{\circ}56'29.58''\text{N}$ and $12^{\circ}25'20.64''\text{E}$ to $12^{\circ}33'46.36''\text{E}$. Cairo extends from $29^{\circ}59'17.37''\text{N}$ to $30^{\circ}05'40.83''\text{N}$ and $31^{\circ}09'54.75''\text{E}$ to $31^{\circ}17'15.55''\text{E}$. Madrid spans $40^{\circ}21'42.09''\text{N}$ to $40^{\circ}28'07.75''\text{N}$ and $3^{\circ}46'34.55''\text{W}$ to $3^{\circ}38'09.95''\text{W}$. Istanbul extends from $41^{\circ}00'05.27''\text{N}$ to $41^{\circ}06'25.35''\text{N}$ and $28^{\circ}57'19.38''\text{E}$ to $29^{\circ}05'41.14''\text{E}$.

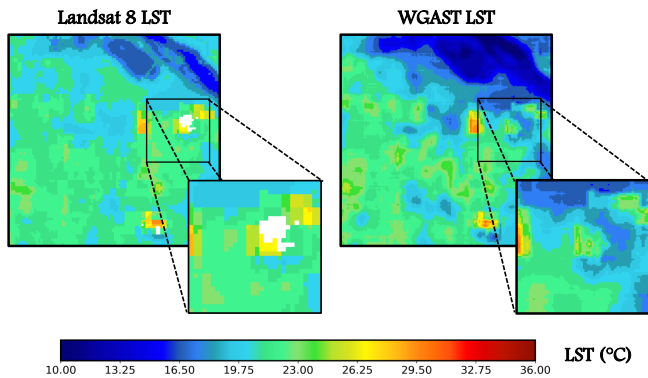


Fig. 10. WGAST reconstruction of cloud-covered area in Landsat 8 LST on 21 Oct 2024. The comparison shows Landsat 8 LST (left column) and the corresponding WGAST LST prediction (right column). Zoomed-in areas highlight regions with missing data in Landsat due to clouds.

Table VII reports the quantitative performance. Tours, climatically similar to Orléans, shows a low RMSE of 1.099 and high SSIM of 0.858. Madrid maintains comparable performance, while Montpellier and Rome exhibit modestly higher RMSEs (1.743 and 1.786, respectively) but remain reliable. In regions with climates markedly different from Orléans, Cairo and Istanbul, RMSE increases (2.689 and 2.767) yet remains moderate and acceptable, especially given that baseline methods recorded higher RMSEs even within the training ROI (Orléans Métropole). Overall, these results confirm WGAST’s strong spatio-temporal generalization across diverse climates and geographies by effectively capturing thermal patterns and fine spatial structures, such as the Loire River in Tours, the Tiber River in Rome, and the Bosphorus Strait in Istanbul, as illustrated in Fig. 11.

TABLE VII
MODEL PERFORMANCE IN NEW REGIONS.

Region	RMSE	SSIM	PSNR	SAM	CC	ERGAS
Tours	1.099	0.858	25.080	2.637	0.899	1.578
Montpellier	1.743	0.793	21.095	2.901	0.791	2.394
Madrid	1.178	0.872	26.192	2.821	0.821	1.702
Rome	1.786	0.829	22.523	2.364	0.817	1.451
Cairo	2.689	0.848	16.429	4.208	0.771	4.211
Istanbul	2.767	0.724	15.712	7.469	0.765	5.156

F. Ablation Study

We focus on evaluating the contribution of input modalities to WGAST’s performance. Specifically, we investigate how the inclusion or exclusion of different spectral indices, NDVI, NDWI, and NDBI, affects the model’s ability to predict daily 10 m LST. For clarity, when we refer to a given index, we include both the 10 m Sentinel-2 and 30 m Landsat 8 indices, along with all associated encoding components in the generator. Table VIII summarizes the results. It is evident that the full combination of NDVI, NDWI, and NDBI yields the best performance across most quantitative metrics, which demonstrates that each index provides complementary information that enhances spatial fidelity, structural accuracy,

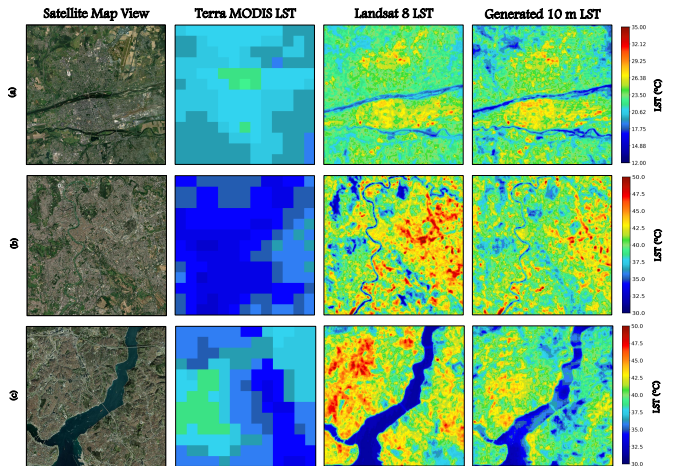


Fig. 11. Visual illustration of WGAST predictions across regions with different climatic characteristics and acquisition dates: (a) Tours (temperate oceanic, 21 Oct 2024), (b) Rome (Mediterranean, 10 Jun 2025), and (c) Istanbul (transitional Mediterranean-continental, 10 Apr 2025).

and spectral consistency. Removing or partially excluding indices generally leads to higher RMSE and ERGAS and lower SSIM and PSNR.

TABLE VIII
ABLATION STUDY ON INPUT MODALITIES.

Input	RMSE	SSIM	PSNR	SAM	CC	ERGAS
NDVI	2.726	0.849	19.468	4.226	0.765	3.657
NDWI	2.375	0.832	19.440	3.624	0.813	3.301
NDBI	2.633	0.855	20.511	4.062	0.829	3.513
NDVI/NDWI	2.082	0.856	22.429	4.101	0.810	2.712
NDVI/NDBI	1.960	0.851	18.903	3.998	0.832	3.724
NDWI/NDBI	2.747	0.845	18.903	3.988	0.803	3.724
NDVI/NDWI/NDBI	1.951	0.865	23.704	4.148	0.830	2.582

V. CONCLUSION

In this work, we introduced WGAST, a weakly-supervised generative network for daily 10 m LST estimation via STF of Terra MODIS, Landsat 8, and Sentinel-2 data. To the best of our knowledge, WGAST is the first fully DL-based framework specifically designed for this task. The framework is built upon a cGAN, where the generator follows a four-stage pipeline: feature extraction, feature fusion, LST reconstruction, and noise suppression. A key contribution lies in using cosine similarity to guide fusion by transferring relevance scores from Sentinel-2 and Landsat 8 spectral features to Landsat 8 LST features. Training is weakly supervised through physical averaging, where the generated 10 m LST is upsampled to 30 m and compared to Landsat 8 LST. WGAST requires only Terra MODIS LST at the target time and a prior triplet T_1 combining Terra MODIS, Landsat 8, and Sentinel-2, thereby preserving daily temporal resolution. WGAST outperforms existing methods both quantitatively and qualitatively. Compared to FuseTen, it achieves on average a 17.05% reduction in RMSE, 4.22% improvement in SSIM, 10.98% increase in PSNR, and 13.76% reduction in ERGAS, with even larger

gains over traditional linear and existing combinations of STF and downscaling methods. It also preserves fine spatial structures such as temperature gradients along rivers and bridges, variations around buildings, and detailed urban and agricultural patterns. Additionally, by relying solely on Terra MODIS LST at the target date, WGAST effectively overcomes cloud-induced gaps in Landsat 8, by producing complete, high-resolution, and physically consistent LST maps. Its robustness is further confirmed by the strong agreement between the generated 10 m LST maps and in situ measurements from 33 near-ground sensors across the ROI.

WGAST demonstrates strong spatio-temporal generalization across diverse regions and climates. However, in areas with climatic conditions that differ substantially from the training region, a noticeable yet moderate performance drop occurs. Future work will focus on developing an inference and transfer learning framework to enable automatic adaptation to unseen regions without requiring full retraining. Furthermore, regarding practical implementation, generating daily 10 m LST with WGAST requires two inputs: Terra MODIS LST at the target date and a reference triplet comprising Terra MODIS, Landsat 8, and Sentinel-2 observations at a nearby date with minimal cloud coverage. Missing pixels are filled using adaptive spatial interpolation. Future direction will explore extending WGAST to explicitly handle incomplete inputs by enabling the model to predict and fill gaps directly during inference.

REFERENCES

- [1] C. Folke *et al.*, "Our future in the anthropocene biosphere," *Ambio*, vol. 50, pp. 834–869, 2021.
- [2] P. Singh, N. Kikon, and P. Verma, "Impact of land use change and urbanization on urban heat island in lucknow city, central india. a remote sensing based estimate," *Sustain. Cities Soc.*, vol. 32, pp. 100–114, 2017.
- [3] B. D. Sparrow *et al.*, "Effective ecosystem monitoring requires a multi-scaled approach," *Biological Reviews*, vol. 95, no. 6, pp. 1706–1719, 2020.
- [4] Y. Chu, M. Ye, and Y. Qian, "Fine-grained image recognition methods and their applications in remote sensing images: A review," *IEEE J. Sel. Topics Appl. Earth Observ. Remote Sens.*, 2024.
- [5] F. Li *et al.*, "Machine learning and remote sensing integration for leveraging urban sustainability: A review and framework," *Sustain. Cities Soc.*, vol. 96, p. 104653, 2023.
- [6] V. V. Estrela *et al.*, "Remote sensing applications in disease mapping and public health analysis," in *Intelligent Healthcare Systems*. CRC Press, 2023, pp. 185–202.
- [7] N. Kerle, "Disasters: Risk assessment, management, and post-disaster studies using remote sensing," in *Remote Sensing Handbook, Volume VI*. CRC Press, 2024, pp. 153–198.
- [8] B. Sirmacek and R. Vinuesa, "Remote sensing and ai for building climate adaptation applications," *Results Eng.*, vol. 15, p. 100524, 2022.
- [9] S. Bouaziz, A. Hafiane, R. Canals, and R. Nedjai, "Deep learning for spatio-temporal fusion in land surface temperature estimation: A comprehensive survey, experimental analysis, and future trends," *arXiv preprint arXiv:2412.16631*, 2024.
- [10] G. C. Hulley *et al.*, "3 - land surface temperature," in *Taking the Temperature of the Earth*, G. C. Hulley and D. Ghent, Eds. Elsevier, 2019, pp. 57–127.
- [11] D. K. Hall *et al.*, "A satellite-derived climate-quality data record of the clear-sky surface temperature of the greenland ice sheet," *Journal of Climate*, vol. 25, no. 14, pp. 4785–4798, 2012.
- [12] S. Luyssaert *et al.*, "Land management and land-cover change have impacts of similar magnitude on surface temperature," *Nature Climate Change*, vol. 4, no. 5, pp. 389–393, 2014.
- [13] M. Maimaitiyiming *et al.*, "Effects of green space spatial pattern on land surface temperature: Implications for sustainable urban planning and climate change adaptation," *ISPRS J. Photogramm. Remote Sens.*, vol. 89, pp. 59–66, 2014.
- [14] M. King, *EOS Science Plan: The State of Science in the EOS Program*. National Aeronautics and Space Administration, 1999.
- [15] R. Hollmann *et al.*, "The esa climate change initiative: Satellite data records for essential climate variables," *Bulletin of the American Meteorological Society*, vol. 94, no. 10, pp. 1541–1552, 2013.
- [16] Z.-L. Li *et al.*, "Satellite-derived land surface temperature: Current status and perspectives," *Remote Sens. Environ.*, vol. 131, pp. 14–37, 2013.
- [17] J. Zhang and J. Li, "Chapter 11 - spacecraft," in *Spatial Cognitive Engine Technology*, J. Zhang and J. Li, Eds. Academic Press, 2023, pp. 129–162.
- [18] P. Gibson, "Chapter 1 - a systematic view of remote sensing (second edition)," in *Advanced Remote Sensing*, S. Liang and J. Wang, Eds. Academic Press, 2020, pp. 1–57.
- [19] X. Zhu *et al.*, "Spatiotemporal fusion of multisource remote sensing data: Literature survey, taxonomy, principles, applications, and future directions," *Remote Sensing*, vol. 10, no. 4, p. 527, 2018.
- [20] H. Song *et al.*, "Spatiotemporal satellite image fusion using deep convolutional neural networks," *IEEE J. Sel. Topics Appl. Earth Observ. Remote Sens.*, vol. 11, no. 3, pp. 821–829, 2018.
- [21] R. Swain, A. Paul, and M. D. Behera, "Spatio-temporal fusion methods for spectral remote sensing: A comprehensive technical review and comparative analysis," *Tropical Ecology*, vol. 65, no. 3, pp. 356–375, 2024.
- [22] F. Gao, J. Masek, M. Schwaller, and F. Hall, "On the blending of the landsat and modis surface reflectance: Predicting daily landsat surface reflectance," *IEEE Trans. Geosci. Remote Sens.*, vol. 44, no. 8, pp. 2207–2218, 2006.
- [23] X. Zhu *et al.*, "An enhanced spatial and temporal adaptive reflectance fusion model for complex heterogeneous regions," *Remote Sens. Environ.*, vol. 114, no. 11, pp. 2610–2623, 2010.
- [24] H. Liu and Q. Weng, "Enhancing temporal resolution of satellite imagery for public health studies: A case study of west nile virus outbreak in los angeles in 2007," *Remote Sens. Environ.*, vol. 117, pp. 57–71, 2012.
- [25] Y. Ma, S. Liu, L. Song, Z. Xu, Y. Liu, T. Xu, and Z. Zhu, "Estimation of daily evapotranspiration and irrigation water efficiency at a landsat-like scale for an arid irrigation area using multi-source remote sensing data," *Remote Sens. Environ.*, vol. 216, pp. 715–734, 2018.
- [26] B. Mohamadi, S. Chen, T. Balz, K. Gulshad, and S. C. McClure, "Normalized method for land surface temperature monitoring on coastal reclaimed areas," *Sensors*, vol. 19, no. 22, p. 4836, 2019.
- [27] Y. Yu *et al.*, "Generating daily 100 m resolution land surface temperature estimates continentally using an unbiased spatiotemporal fusion approach," *Remote Sens. Environ.*, vol. 297, p. 113784, 2023.
- [28] J. Gao, H. Sun, Z. Xu, T. Zhang, H. Xu, D. Wu, and X. Zhao, "Cpmf: An integrated technology for generating 30-m, all-weather land surface temperature by coupling physical model, machine learning and spatiotemporal fusion model," *IEEE Trans. Geosci. Remote Sens.*, 2024.
- [29] Z. Yin *et al.*, "Spatiotemporal fusion of land surface temperature based on a convolutional neural network," *IEEE Trans. Geosci. Remote Sens.*, vol. 59, no. 2, pp. 1808–1822, 2020.
- [30] Y. Chen *et al.*, "Spatiotemporal fusion network for land surface temperature based on a conditional variational autoencoder," *IEEE Trans. Geosci. Remote Sens.*, vol. 60, pp. 1–13, 2022.
- [31] P. Hu, X. Pan, Y. Yang, Y. Dai, and Y. Chen, "A two-stage hierarchical spatiotemporal fusion network for land surface temperature with transformer," *IEEE Trans. Geosci. Remote Sens.*, 2025.
- [32] I. Goodfellow *et al.*, "Generative adversarial nets," *Advances in neural information processing systems*, vol. 27, 2014.
- [33] H. Zhang, Y. Song, C. Han, and L. Zhang, "Remote sensing image spatiotemporal fusion using a generative adversarial network," *IEEE Trans. Geosci. Remote Sens.*, vol. 59, no. 5, pp. 4273–4286, 2020.
- [34] Z. Tan *et al.*, "A flexible reference-insensitive spatiotemporal fusion model for remote sensing images using conditional generative adversarial network," *IEEE Trans. Geosci. Remote Sens.*, vol. 60, pp. 1–13, 2021.
- [35] J. Chen, L. Wang, R. Feng, P. Liu, W. Han, and X. Chen, "Cyclegan-stf: Spatiotemporal fusion via cyclegan-based image generation," *IEEE Trans. Geosci. Remote Sens.*, vol. 59, no. 7, pp. 5851–5865, 2020.
- [36] B. Song *et al.*, "Mlff-gan: A multilevel feature fusion with gan for spatiotemporal remote sensing images," *IEEE Trans. Geosci. Remote Sens.*, vol. 60, pp. 1–16, 2022.
- [37] P. Wu *et al.*, "Spatially continuous and high-resolution land surface temperature product generation: A review of reconstruction and spatiotemporal fusion techniques," *IEEE Geosci. Remote Sens. Mag.*, vol. 9, no. 3, pp. 112–137, 2021.

- [38] A. Prata *et al.*, “Thermal remote sensing of land surface temperature from satellites: Current status and future prospects,” *Remote sensing reviews*, vol. 12, no. 3-4, pp. 175–224, 1995.
- [39] D. P. Roy *et al.*, “Landsat-8: Science and product vision for terrestrial global change research,” *Remote Sens. Environ.*, vol. 145, pp. 154–172, 2014.
- [40] H. Shi *et al.*, “Urban heat island and its regional impacts using remotely sensed thermal data—a review of recent developments and methodology,” *Land*, vol. 10, no. 8, p. 867, 2021.
- [41] D. Zhou *et al.*, “Satellite remote sensing of surface urban heat islands: Progress, challenges, and perspectives,” *Remote Sensing*, vol. 11, no. 1, p. 48, 2018.
- [42] M. Mhaweji and Y. Abunnasr, “Daily ten-st-gee: An open access and fully automated 10-m 1st downscaling system,” *Computers & Geosciences*, vol. 168, p. 105220, 2022.
- [43] D. Xiang *et al.*, “Comparative analysis of prediction models for trawling grounds of the argentine shortfin squid *illux argentinus* in the southwest atlantic high seas based on vessel position and fishing log data,” *Biology*, vol. 14, no. 1, p. 35, 2025.
- [44] S. Bouaziz, A. Hafiane, R. Canals, and R. Nedjai, “Fuseten: A generative model for daily 10 m land surface temperature estimation from spatio-temporal satellite observations,” in *2025 International Conference on Machine Intelligence for GeoAnalytics and Remote Sensing (MIGARS)*, 2025, pp. 1–4.
- [45] S. Guha, H. Govil, A. K. Taloor, N. Gill, and A. Dey, “Land surface temperature and spectral indices: A seasonal study of raipur city,” *Geodesy and Geodynamics*, vol. 13, no. 1, pp. 72–82, 2022.
- [46] A. J. Abdalkadhum, M. M. Salih, and O. Z. Jasim, “The correlation among land cover spectral indices and surface temperature using remote sensing techniques,” in *IOP Conference Series: Materials Science and Engineering*, vol. 1090, no. 1. IOP Publishing, 2021, p. 012024.
- [47] P. Sharma, M. Kumar, H. K. Sharma, and S. M. Biju, “Generative adversarial networks (gans): Introduction, taxonomy, variants, limitations, and applications,” *Multimedia Tools and Applications*, pp. 1–48, 2024.
- [48] Y. Hong, U. Hwang, J. Yoo, and S. Yoon, “How generative adversarial networks and their variants work: An overview,” *ACM Computing Surveys (CSUR)*, vol. 52, no. 1, pp. 1–43, 2019.
- [49] Y.-P. Hsieh, C. Liu, and V. Cevher, “Finding mixed nash equilibria of generative adversarial networks,” in *International Conference on Machine Learning*. PMLR, 2019, pp. 2810–2819.
- [50] M. Mirza and S. Osindero, “Conditional generative adversarial nets,” *arXiv preprint arXiv:1411.1784*, 2014.
- [51] C. He *et al.*, “Diffusion models in low-level vision: A survey,” *IEEE Transactions on Pattern Analysis and Machine Intelligence*, 2025.
- [52] B. Lim, S. Son, H. Kim, S. Nah, and K. Mu Lee, “Enhanced deep residual networks for single image super-resolution,” in *Proc. IEEE Conf. Comput. Vis. Pattern Recognit. workshops*, 2017, pp. 136–144.
- [53] X. Huang and S. Belongie, “Arbitrary style transfer in real-time with adaptive instance normalization,” in *Proc. IEEE Int. Conf. Comput. Vis.*, 2017, pp. 1501–1510.
- [54] L. Gao *et al.*, “Localization or globalization? determination of the optimal regression window for disaggregation of land surface temperature,” *IEEE Trans. Geosci. Remote Sens.*, vol. 55, no. 1, pp. 477–490, 2016.
- [55] Z.-H. Zhou, “A brief introduction to weakly supervised learning,” *National science review*, vol. 5, no. 1, pp. 44–53, 2018.
- [56] X. Mao *et al.*, “Least squares generative adversarial networks,” in *Proc. IEEE Int. Conf. Comput. Vis.*, 2017, pp. 2794–2802.
- [57] N. Gorelick *et al.*, “Google earth engine: Planetary-scale geospatial analysis for everyone,” *Remote Sens. Environ.*, vol. 202, pp. 18–27, 2017.
- [58] S.-B. Duan *et al.*, “Validation of collection 6 modis land surface temperature product using in situ measurements,” *Remote Sens. Environ.*, vol. 225, pp. 16–29, 2019.
- [59] J. C. Jimenez-Munoz *et al.*, “Land surface temperature retrieval methods from landsat-8 thermal infrared sensor data,” *IEEE Geosci. Remote Sens. Lett.*, vol. 11, no. 10, pp. 1840–1843, 2014.
- [60] Z. Tan *et al.*, “An enhanced deep convolutional model for spatiotemporal image fusion,” *Remote Sensing*, vol. 11, no. 24, p. 2898, 2019.
- [61] M. Naserikia *et al.*, “Land surface and air temperature dynamics: The role of urban form and seasonality,” *Science of The Total Environment*, vol. 905, p. 167306, 2023.
- [62] P. Sedgwick, “Pearson’s correlation coefficient,” *Bmj*, vol. 345, 2012.
- [63] J. H. Zar, “Spearman rank correlation: overview,” *Wiley StatsRef: Statistics Reference Online*, 2014.



Sofiane Bouaziz is PhD Student at INSA Centre Val de Loire (INSA CVL) and the PRISME Laboratory. He received his Master’s and Engineering degrees in Computer Science and Artificial Intelligence from École Nationale Supérieure d’Informatique, Algiers, Algeria in 2023. His current research focuses on using Artificial Intelligence and Computer Vision to tackle challenges in remote sensing.



Adel Hafiane received the M.S. degree in embedded systems and information processing, and the Ph.D. degree from the University of Paris-Saclay, in 2002 and 2005, respectively. He subsequently spent a year engaged in teaching and research. This followed by postdoctoral position at the computer science department, University of Missouri, from 2007 to 2008. Since September 2008, he joined INSA CVL as associate professor and later the university of Orléans in 2025. He is a head of the Image and Vision Group at the PRISME Laboratory, a joint research unit of the University of Orléans and INSA CVL. He was an invited researcher at the University of Missouri on multiple periods, from 2009 to 2013. His research interests include theory and methods of machine learning and computer vision for different applications. He coordinated several research projects and co-authored more than 90 papers and 3 patents. He has also served as an associate editor for several special issues.



Raphaël Canals received the Dipl.Ing. degree in electrical engineering and the Ph.D. degree in electronics from the University of ClermontFerrand, France, in 1989 and 1993, respectively. In 1993, he was Postdoctoral Fellow at the Computer Science Department, CNRC, Ottawa, ON, Canada. In 1994, he joined the Polytechnic School, University of Orléans, France, as a Teacher. He is currently a Researcher with Laboratory PRISME, University of Orléans-INSA CVL. He is also an Associate Professor with the University of Orléans. In 2015, he was introduced at the AgreenTech Valley Cluster dedicated to digital technologies for plant industry. His current interests are in biomedical imaging, innovation for agriculture, the IoT, and AI.



Rachid Nedjai is a professor in limnology and geomatics at the University of Orléans, where he also leads the Master’s program in Geographic Information Systems (GAED). He obtained his Ph.D. in geochemistry of lacustrine waters and paleoenvironmental reconstruction from the University of Grenoble 1. His research focuses on environmental data simulation, hydrogeology, and geomatics applications for water resource management. He has contributed to numerous international projects, including the redesign of Algeria’s judicial map and a spatial data infrastructure for water management in Africa. He has supervised multiple theses on hydrology, water resource management, and environmental risk assessment, with many of his students successfully entering the professional world. His expertise in geomatics and water resource management has made him a key contributor to advancing sustainable practices in the field.